



# Integrated sensor printed on the separator enabling the detection of dissolved manganese ions in battery cell

Tina Paljk<sup>a,b</sup>, Victoria Bracamonte<sup>c</sup>, Tomáš Syrový<sup>d</sup>, Sara Drvarič Talian<sup>a</sup>, Samo Hočevár<sup>a</sup>, Robert Dominko<sup>a,b,e,\*</sup>

<sup>a</sup> National Institute of Chemistry, Hajdrihova 19 SI, Ljubljana1000, Slovenia

<sup>b</sup> Faculty of Chemistry and Chemical Technology, University of Ljubljana, Večna pot 113 SI, Ljubljana 1000, Slovenia

<sup>c</sup> Facultad de Matemática, Astronomía, Física y Computación, Universidad Nacional de Córdoba, Av. Haya de la Torre s/n, Córdoba, Argentina

<sup>d</sup> Faculty of Chemical Technology, Department of Graphic Arts and Photophysics, University of Pardubice, Doubravice 41, Pardubice 53353, Czech Republic

<sup>e</sup> Alistore ERI, Amiens, France

## ARTICLE INFO

### Keywords:

Li-ion battery  
Mn dissolution  
Sensor  
Printing technology  
Impedance spectroscopy

## ABSTRACT

Conventional monitoring of Li-ion battery cell performance is carried out by combining empirical measurement of the extrinsic parameters with multipart modeling and approximation algorithms. A step forward would be enabling more reliable built-in sensing systems that allow collecting direct information, such as a degree of constituting materials degradation. Transition metal dissolution is one of the most severe degradation processes affecting the performance of the whole battery cell. It can be accelerated through different mechanisms, and its monitoring has been a topic of several studies in recent decades. In this work, we establish an approach for unambiguous detection of dissolved manganese ions via the built-in electrochemical sensor with scavenger moieties. We demonstrate that manganese ion-imprinted polymer (Mn(II)-IIP) deposited between two electrodes printed directly on the separator can be used as a sensing layer. The resistance of this sensing layer changes due to the coordination of the ion-imprinted polymer with dissolved manganese ions and this is then precisely monitored by the electrochemical impedance spectroscopy in the mid-frequency range. Both the electrodes and sensing layer remain stable within the voltage range of battery cycling over a longer application time. The sensor performance was validated in the single-layer pouch cell using Li||LiMn<sub>2</sub>O<sub>4</sub> chemistry. The use of printing technology permits large-scale commercialization; sensors printed on the separator do not significantly alter the current production technology and, most importantly, have a negligible impact on the cell energy density. The approach is universal and can eventually be extended to the detection of other degradation products in the electrolyte.

## 1. Introduction

Lithium-ion batteries (LIBs) play an essential role in the green transition towards the efficient use of renewable energy and electrification in numerous sectors. Their performance is monitored with a battery management system (BMS) and relies on complex analysis and models based on external parameters: voltage (V), current (I), and resistance (R) [1]. Further improvement of the quality, reliability, lifetime and safety (QRSL) could be obtained by the introduction of smart functionalities into the battery cell [2]. Continuous (*operando* mode) or occasional monitoring (*in situ* mode) of additional parameters such as temperature, pressure, strain, and electrolyte composition can provide a piece of

valuable information about the state of health (SoH) and state of safety (SoS) within the individual cell [2].

The quest to successfully embed smart functionalities in a battery cell requires adaptability and miniaturization of already existing [3–8] or completely novel technologies. Sensors, as a vital part of smart functionalities, should be stable, cheap, and reliable over a long period [8]. Many different analytical methods have been applied as *in situ* and/or *operando* characterization techniques to better understand battery degradation mechanisms [4–7,9]. Many of them are less viable for monitoring commercial cells due to sophisticated instrumentation and specific cell arrangements [4–7].

Among the most significant advances so far achieved in monitoring

\* Corresponding author at: National Institute of Chemistry, Hajdrihova 19 SI, Ljubljana1000, Slovenia.

E-mail address: [robert.dominko@ki.si](mailto:robert.dominko@ki.si) (R. Dominko).

<https://doi.org/10.1016/j.ensm.2022.11.039>

Received 20 September 2022; Received in revised form 30 October 2022; Accepted 20 November 2022

Available online 21 November 2022

2405-8297/© 2022 The Author(s). Published by Elsevier B.V. This is an open access article under the CC BY-NC-ND license (<http://creativecommons.org/licenses/by-nc-nd/4.0/>).

battery cells is the determination of the temperature at the surface and within the cell [3,10–17]. Another type of battery diagnostic involves the determination of strain and pressure changes by gauge sensors [18–20]. Other possible solutions are represented by families of nano-plasmonic sensors [21], acoustic sensors [22], and electrochemical sensors.

Electrochemical sensing can provide real-time information about electrochemical changes by introducing one or more additional electrodes into the battery cell [3]. The use of a simple reference electrode enables the detection of polarization on both electrodes, while the detection of chemical changes requires two or more additional electrodes. This approach has been demonstrated on lab-scale battery cells [23–25]. Such electrochemical sensors are promising, particularly in the fields of biophysics and biochemistry, since they can be easily miniaturized and integrated into automated production while retaining their analytical properties [26].

To maximize their utility, electrochemical sensors should be designed in a way enabling the detection of a process that is the most detrimental to the battery. Cathode degradation with transition metal (TM) dissolution is one of the major reasons for capacity degradation in LiBs [27]. Among all, manganese dissolution in manganese-containing cathode materials seems to be the most unfavorable since it causes structural changes in the cathode and influences the properties of the solid electrolyte interface (SEI) on the anode surface [28].

Manganese dissolution has been intensively investigated [29,28], but there are still numerous open questions about the mechanism and the oxidation state of the manganese ions inside the electrolyte. Hunter et al. reported that the major reason for the severe manganese dissolution from spinel  $\text{LiMn}_2\text{O}_4$  is due to acidic conditions in the electrolyte, which can be induced by traces of water [30]. The disproportionation reaction ( $2\text{Mn}^{3+} \rightarrow \text{Mn}^{4+} + \text{Mn}^{2+}(\text{soln})$ ) for the  $\text{LiMn}_2\text{O}_4$  cathode material was proposed by Gummow et al. [31] These reactions can be accelerated by high temperatures and a large surface area of the cathode material [32–35]. Another source of dissolved manganese ions can be the dissolution of trivalent cations at high potentials [36,37].

*In situ* detection of TM ions and the direct connection between *SoH* and dissolved quantity of TMs is a subject of various studies. Terada et al. used a capillary tube for sampling the battery electrolyte during cell cycling [38]. The sampled electrolyte was analyzed by the total reflection X-ray fluorescence technique. Wang et al. studied manganese dissolution by using a rotating ring disk electrode (RRDE) [39]. Zhao et al. directly measured the manganese ion concentration using a UV–vis probe [40], Banerjee et al. used electronic paramagnetic resonance (EPR) combined with inductively coupled plasma (ICP) spectroscopies [36]. More recently, Hanf et al. quantified manganese species using a new capillary electrophoresis (CE) method with ultraviolet-visible detection [41], and Nikman et al. employed a droplet flow cell-inductively coupled plasma optical emission spectrometer (ICP-OES) set-up [42]. In all studies, a reliable quantification of manganese dissolved in the electrolyte was demonstrated; however, all studies require a modification of the battery cell. In a recent paper, Wang et al. proposed a Swagelok T-cell with three additional electrodes to detect manganese and determine polarization between electrodes [24]. The setup included a Pt mesh sensing electrode located between the battery cathode and anode, and an  $\text{Ag}/\text{Ag}^+$  reference electrode. Setting the potential of the Pt sensing electrode to 1.0 V versus the  $\text{Ag}/\text{Ag}^+$  reference electrode allowed *in situ* detection of manganese dissolution from the  $\text{LiMn}_2\text{O}_4$  electrode. Although reliable detection of dissolved manganese and other TMs has been reported, the proposed methodologies exhibit several limitations for scaling up to the industrial level.

Through the extensive testing of Mn dissolution influence on battery performance we clearly demonstrate the importance of building a reliable sensor for monitoring transition metals dissolution from electrode material. An electrochemical sensor demonstrated in this work that is integrated into the battery separator serves as an *in situ* analytical tool

for the detection of dissolved manganese in the battery cell. The sensor is prepared by printing technology enabling large-scale commercialization due to the possibility of producing sensors using a sheet-to-sheet or roll-to-roll process [43–48]. The sensor is positioned between the negative and positive electrodes without significantly changing the geometry of the battery cell and negligibly affecting its performance. The coordination of dissolved manganese ions can be effectively monitored by electrochemical impedance spectroscopy (EIS). The proof of concept was demonstrated in a laboratory-size pouch  $\text{LMO}|\text{Li}$  battery cell.

## 2. Materials and methods

### 2.1. Materials

All sensors and cell setups were prepared in an argon-filled glovebox (MBRAUN,  $\text{O}_2 < 1.0$  ppm,  $\text{H}_2\text{O} < 1.0$  ppm) with previously dried components.

The manganese ion-imprinted polymer (Mn(II)-IIP) was prepared by thermal-initiated radical polymerization according to the procedure published in Roushani et al. [49]. The Mn(II)-IIP is based on a 1-(2-pyridylazo)–2-naphthol (PAN, Merck) chelating agent for divalent cations. The additional chemicals used for the synthesis of the ion-imprinted polymer were: methacrylic acid (MAA, 99%, 250 ppm of Monomethyl Ether of Hydroquinone (MEHQ) as the inhibitor, Aldrich) as the monomer, ethylene glycol dimethacrylate (EGDMA, 98%, 90–110 ppm MEHQ as the inhibitor) as the crosslinker, 2,2'-azobisisobutyronitrile (AIBN, 98%, Sigma-Aldrich) as the initiator, manganese(II) chloride tetrahydrate (99+%, Sigma Aldrich) as the source of template manganese(II), and methanol (99%, J.T. Baker) and ethanol (99.9%, Carlo Erba) as the solvents. The resulting polymer was washed with 6.0 M hydrochloric acid (prepared from 37% HCl, Carlo Erba) and deionized water to leach the template ions.

Cyclic voltammetric (CV) measurements were carried out to check the electrochemical stability of the Mn(II)-IIP sensing material. Tests were performed in a two-electrode pouch cell using glassy carbon (GC, HTW) and lithium metal electrodes (thickness 110  $\mu\text{m}$ , FMC), both with a surface of 1  $\text{cm}^2$ . The GC electrode was used as received, or it was coated by drop-casting a solution of Mn(II)-IIP and PVdF (polyvinylidene fluoride, average molar mass 543,000, Sigma Aldrich) in NMP (N-methyl-2-pyrrolidone, 99+%, Sigma Aldrich) in the weight ratio 1:1:25. Electrodes were separated with a layer of Celgard™ 2320 (20 mm in diameter) separator wetted with 20  $\mu\text{L}$  of electrolyte. Two different electrolytes were used, i.e., a standard one of 1.0 M  $\text{LiPF}_6$  in 1:1 solution of ethylene carbonate (EC) and diethyl carbonate (DEC) (battery grade, Elyte innovation) or the same composition with added 10.0 mM of Manganese(II) acetylacetonate ( $\text{Mn}(\text{AcAc})_2$ , Sigma Aldrich).

The sensor was prepared by printing the GC symmetrical electrodes on a glass fiber substrate (Fisherbrand™ glass fiber circles, thickness 0.32 mm, particle retention 1.6  $\mu\text{m}$ ) with a micro dispensing printing technique (nScript, 3Dn-Tabletop). First, we printed the current collectors' two straight-line parts and two contact pads using silver-based ink, as shown in Fig. 1. The ink consisted of silver flakes with an average diameter of 8  $\mu\text{m}$  (Sigma Aldrich) and a combination of a water-soluble polymer (CMC  $M_w$  250 000, Sigma Aldrich), and an SBR dispersion (MTI Corporation) as the binder. The used weight ratio of silver flakes to the binder dual system was 5.7:0.5:0.5. The silver current collectors were printed at a speed of 400 mm/min, dried at 80 °C for 10 min, then cured at 125 °C for 30 min. In the next step, the circular part of the sensor electrodes was printed with a gap of 0.5 mm using glassy carbon (GC) based ink (Fig. 1a). The ink consisted of glassy carbon particles (Sigma Aldrich) and the same binding system as silver ink. The weight ratio between GC:CMC:SBR was 4.3:0.3:0.7. The GC electrodes were printed at the speed of 300 mm/min and dried at 80 °C for 10 min, followed by curing at 125 °C for 30 min.

The circular part of the sensor has an external diameter of 12 mm (external GC electrode) and an internal diameter of 10 mm (internal GC

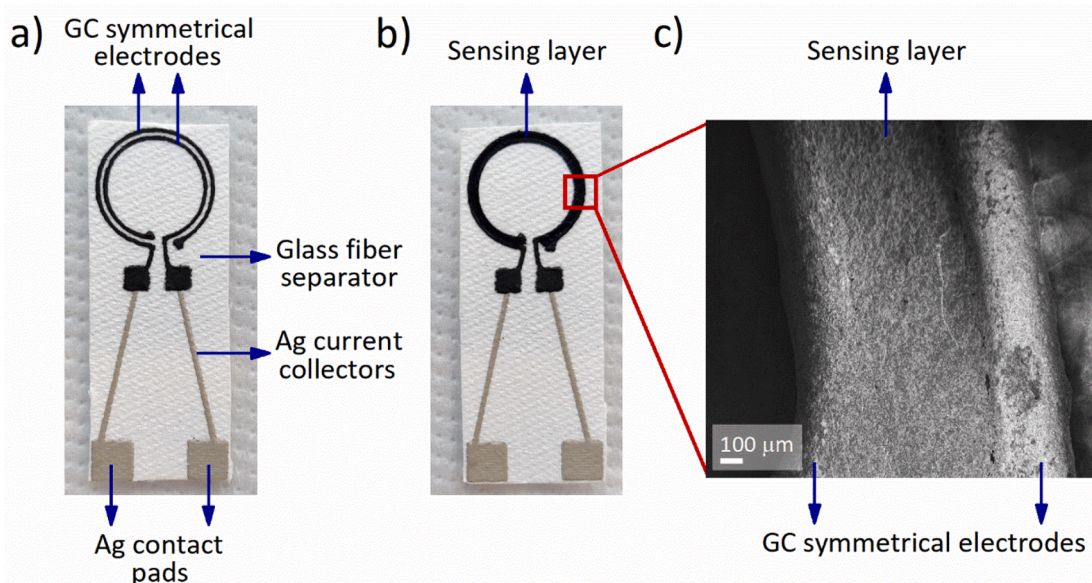


**Fig. 1.** Printed sensor. Photos of the sensor electrodes printed on a glass fiber substrate (a) without and (b) with composite sensing layer; (c) SEM image of the sensor where the GC printed electrodes and the Mn(II)-IIP/MWCNT/PVdF composite sensing layer is visible.

electrode). The gap between the two symmetrical GC electrodes is around 0.5 mm and is modified by the composite sensing layer by drop casting methodology. The circular part is prolonged into two straight rays of about 2 cm in length and is terminated with two contact pads of  $4 \times 4 \text{ mm}^2$ . The two pads are required for wiring the sensor with external nickel terminals.

The Mn(II)-IIP-based sensing layer was prepared using the following procedure: First, we prepared a homogeneous suspension of 10 mg Mn(II)-IIP and 50 mg c-grade MWCNT (Timcal) in NMP solvent. The mixture was then filtered and dried overnight at  $50^\circ\text{C}$ . The resulting composite was dispersed into a 1500 mg solution of PVdF in NMP (weight ratio 1:25). The resulting slurry was manually drop-casted into the gap between the two printed GC electrodes. The sensor was dried at  $80^\circ\text{C}$  for 6 h.

The measurement setup consisted of a pouch bag with two nickel current strips for connecting the sensor to the potentiostat/galvanostat with the electrochemical impedance spectroscopy (EIS) analyzer. The sensor was soaked with  $200 \mu\text{L}$  of  $1.0 \text{ M LiPF}_6$  in EC:DEC 1:1 as electrolyte or with the electrolyte containing  $10.0 \text{ mM Mn}(\text{AcAc})_2$  or  $20.0 \text{ mM}$  of lithium acetylacetonate (LiAcAc, Sigma Aldrich). Finally, the sensor was placed inside the pouch bag, connected with the current collectors, and sealed.

The cathode composite material LMO ( $\text{LiMn}_2\text{O}_4$ , cathode powder SP30, Merck) was mixed in a planetary ball mill (PM100, Retch) with conductive carbon black SUPER C45 and PVdF in NMP, in the ratio of 82:9:9 wt.%. The slurry was cast on a carbon-coated aluminum foil using a doctor blade applicator. The cathode composite was dried overnight at  $80^\circ\text{C}$ . Cathodes with diameters of 12 and 16 mm were cut out and pressed under the external load of 250 Pa for 15 s.

Inductively coupled plasma-mass spectrometry (ICP-MS) was used for the determination of manganese dissolution during chemical or electrochemical aging. Samples were prepared using LMO electrodes (16 mm in diameter) wetted with  $7 \mu\text{L}$   $1.0 \text{ M LiPF}_6$  in EC:DEC 1:1 per mg of LMO material. Lithium foil (16 mm in diameter, thickness of  $110 \mu\text{m}$ , FMC) was used as the anode and two sheets of Celgard™ 2320 (20 mm in diameter) as the separator. The battery cells were packed in a pouch bag (triplex foil with aluminum and copper terminals) and cycled at a rate of 0.33 C. The cycled battery cells were disassembled directly after the electrochemical or chemical aging in the discharge mode for a specific time. The lithium metal anode and the two Celgard™ 2320 separator

sheets were taken from the cell. The lithium metal anode was immersed and dissolved in 2.0 mL ethanol, and both separator sheets were immersed in a 3.0 M solution of  $\text{H}_2\text{SO}_4$  (prepared from 96% sulfuric acid, Carlo Erba) in ethanol for two days. The samples were stored in 2.0 mL vials. After that, the samples were analyzed by ICP-MS. The measurements were carried out using an inductively coupled plasma elemental mass spectrometer (Agilent 7500ce Series) equipped with an octopole collision cell. The samples were diluted ten times in a glass flask containing 1.0 mL sample + 0.1 mL of  $\text{HNO}_3$  (65%, Merck, Darmstadt) + 0.05 mL of  $10 \text{ mg L}^{-1}$  IS (Y, Sc, Ge, Gd, Merck, Darmstadt), and filled with Milli-Q ultrapure water (Millipore, Bedford, MA, USA) to 10.0 mL. The ICP-MS elemental analysis was also used to characterize the leached and unleached Mn(II)-IIP sensing material during its preparation; 3.5 mg of each sample was dissolved in 2.0 mL ethanol stored in 2.0 mL vials before measurement.

The case study cell setup consisted of a pouch battery cell with an integrated new sensor. We prepared a pouch bag with four terminals. Two of them were connected to the cell current collectors for the battery, i.e., a copper foil terminal for the negative lithium electrode and an aluminum foil terminal for the positive LMO electrode. The two other terminals were made from nickel foil and were used for connecting the sensor that was located between two Celgard™ 2320 separator sheets (20 mm in diameter). The sensor and the separators were soaked with  $250 \mu\text{L}$  of  $1.0 \text{ M LiPF}_6$  in EC:DEC 1:1 electrolyte. The sensor was located between the two separators to prevent direct (electrical) contact with battery electrodes. The such setup enables optimal positioning of the sensor in the region where the manganese dissolution should take place. As a reference, we use a pristine glass fiber sheet without any printed structure between two Celgard™ 2320 separators.

## 2.2. Electrochemical measurements

Electrochemical measurements were performed at room temperature using a Biologic VMP3 galvanostat/potentiostat. All battery cells were cycled in the galvanostatic mode between 3.50 and 4.35 V vs.  $\text{Li/Li}^+$  at a fixed charge/discharge current density of 0.33 or 0.10 C. The cyclic voltammetric tests were carried out at a scan rate of  $10 \text{ mV s}^{-1}$  (two cycles) in the range of 3.50 V to 4.35 V vs.  $\text{Li/Li}^+$ , for each studied system. The impedance spectra of the sensor were measured at open circuit potential (OCP) in a frequency range between 1 MHz and 10 mHz

with 10 points per decade with an amplitude of 10 mV (rms). The EIS measurements of the sensor soaked in the electrolyte were taken every 30 min. The EIS measurements of the sensor inside the battery cell were carried out before battery cycling or after the cells had been galvanostatically discharged at the specified cycle and relaxed for 10 min.

### 2.3. SEM and ATR-IR spectroscopy

The morphology of the sensor was checked before use, after being exposed to the electrolyte, and after use in the battery cell by using a scanning electron microscope (FESEM, SUPRA 35VP, Zeiss, Germany). The battery cells were disassembled inside the glovebox, and each sensor was washed with dry DEC to remove any salt residue present on the surface. The samples were transferred to the scanning electron microscope in a homemade holder that enables the transfer of the sample between the glove box and microscope in the protective atmosphere. The accelerating voltage for scanning electron microscopy (SEM) analysis was 1.00 kV.

All ATR-IR measurements took place in an argon-filled glovebox ( $O_2 < 1.0$  ppm,  $H_2O < 1.0$  ppm) with previously dried components. The measurements were conducted on Bruker Alpha II equipped with a Ge crystal ATR and a DTGS detector. The spectra were collected in ATR mode with 64 scans at a resolution of  $2\text{ cm}^{-1}$  in the range of 4000 to  $600\text{ cm}^{-1}$  and analyzed by the software OPUS version 7.8.

## 3. Results and discussion

### 3.1. Manganese dissolution

To correlate the dissolution of manganese with the capacity fade during the electrochemical and chemical cell aging in the discharged state, we run LMO||Li cells at 0.33 C for a different number of cycles. We assembled and cycled six LMO||Li cells in parallel for each data point shown in Fig. 2. Battery cells were assembled by using electrodes from the same batch with loadings close to each other. During cycling, the cells were stopped at discharge mode after the 10th, 25th, 50th, 75th, and 100th cycles. These cells were used to determine the amount of dissolved manganese due to electrochemical aging.

To test the manganese dissolution due to chemical aging, an additional set of three cells was assembled under the same conditions and run for ten complete charge/discharge cycles. The cells were left at OCP in full discharge mode for a different number of days, i.e., 3, 5, 10, and 20 days. For the resting period, three parallel cells were tested; these cells were used to determine the amount of dissolved manganese due to chemical aging. After finishing the aging tests, we carefully opened each cell; separators and lithium metal electrodes were further used for the ICP-MS analysis of manganese. The amount of manganese measured by the ICP-MS is a sum of manganese determined in the separator and on the metallic lithium. A standard deviation of the ICP-MS measurements can be attributed to the manual assembly of battery cells and non-homogenous electrolyte distribution, i.e., the electrolyte that remained in the cathode was not considered for the analysis.

The average capacity fading as a function of cycle number is shown in Fig. 2a (blue circles). The capacity decreased by about 13% after 100 cycles. The capacity fade is almost a linear process with the cycle number. The total amount of manganese determined by the ICP-MS as a sum of quantities obtained from the separator and anode sample at the corresponding cycle number resembles more as a logarithmic function with a cycle number, as shown in Fig. 2a (red circles). This can be explained by the faster kinetics of leaching from the surface compared to the bulk of particles. In addition, separated quantities from the metallic anode and separator are shown in Fig. S1a and S1b in the Supporting Information. The amount of leached manganese found in the separator is about two times higher than that determined from the lithium metal. The total amount of leached manganese was determined to be approximately between 5 and  $15\text{ }\mu\text{g}$ . If compared to the initial mass of

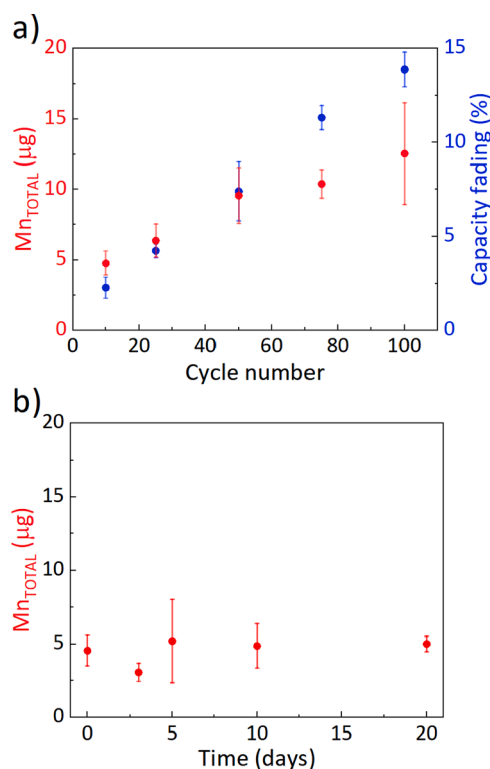


Fig. 2. Transition metal dissolution. (a) Capacity fading as function of cycle number for the LMO||Li cells cycled at 0.33 C between 3.50 and 4.35 V vs.  $Li/Li^+$  (blue) and the total amount of manganese measured by ICP-MS for the batteries stopped at different cycles (red), and (b) the total amount of manganese measured by ICP-MS for the batteries stopped after 10 cycles in discharged state and left to rest for different periods.

manganese inside the cathodic active material, the amount of dissolved manganese is between 0.2 and 0.6% of the original manganese within the LMO. The dependence of the amount of leached manganese as a function of chemical aging in the discharged state is demonstrated in Fig. 2b. The changes in the mass of dissolved manganese are within the experimental error, and the obtained values are consistent with reports in the literature [35,50–54].

Results presented in Fig. 2 suggest that considerable amounts of manganese can be detected in the separator and on the negative lithium electrode in the case of the  $LiMn_2O_4$  cathode. Manganese is considered a sustainable element, and due to high expectations for the future development of manganese-based cathode materials, there is an obvious need for quantitative and qualitative control of manganese dissolution within the battery cell.

### 3.2. Electrochemical sensor setup and characterization

The newly developed sensing platform offers great potential for the detection of dissolved manganese (and some other transition metals) with the sensor integrated into the separator. As shown in Fig. 1, the main components of the sensor are the electrodes and the sensing layer deposited between electrodes with the capability of coordinating divalent manganese ions. A more detailed morphology of the electrodes and sensing layer is depicted in SEM micrographs in Fig. S2.

To test the reproducibility of the drop-casting methodology for the preparation of the sensing layer, we measured each sensor's resistance under ambient conditions. Due to the manual addition of the sensing layer between electrodes, we observed some variations in overall resistance between sensors in the range of 2.7 and 4.5 k $\Omega$ .

The active compound in the sensing layer is Mn(II)-IIP which is an ion-imprinted polymer based on the PAN ligand as a strong organic

reagent for chelating metal ions. The bonding of the metal ions involves two PAN molecules arranged around one metal cation, creating the  $\text{M-PAN}_2$  complex. The as-prepared active material contains manganese, which is removed from the structure by leaching with diluted hydrochloric acid. Structures of the  $\text{Mn(II)-IIP}$  bonding site before and after the leaching of manganese are shown in Fig. 3a. The ATR-IR spectra confirmed the preparation of  $\text{Mn(II)-IIP}$ , and the IR spectra of leached and unleached-IIP (Fig. S3) are in good agreement with the IR absorption bands and shifts, as reported by Roushani et al. [49]. The spectrum of unleached  $\text{Mn(II)-IIP}$  shows absorption bands for stretching vibrations of  $\text{C=N}$  and  $\text{C=O}$  at  $1630\text{ cm}^{-1}$  and  $1727\text{ cm}^{-1}$ , respectively. In the ATR-IR spectrum of the leached  $\text{Mn(II)-IIP}$ , the stretching vibration for  $\text{C=N}$  functional group is shifted to a higher wavenumber,  $1638\text{ cm}^{-1}$ , while the vibration for the  $\text{C=O}$  functional group instead remains at  $1727\text{ cm}^{-1}$ . The shift in the  $\text{C=N}$  stretching vibration implies that the imprinted ion has been sufficiently rinsed from the polymer. Additional IR characterization of the sensing layer is shown in SI in Fig. S4. From Fig. S4 is visible that the  $\text{Mn(II)-IIP}$  IR bands match with the bands in the  $\text{Mn(II)-IIP/MWCNT}$  composite and the final sensing layer. Both the spectra in (b) show an additional IR band around  $1680\text{ cm}^{-1}$  due to  $\text{C=O}$  stretching vibrations, which corresponds to the NMP solvent residuals in the sample. Comparing the spectra of the sensing layer spectra to the  $\text{Mn(II)-IIP/MWCNT}$ , we can see an increase in the IR band at  $1400\text{ cm}^{-1}$  and two additional IR bands at  $1070\text{ cm}^{-1}$  and  $875\text{ cm}^{-1}$  caused by the presence of the PVdF binder. We can also see a shift in the IR band  $1147\text{ cm}^{-1}$  (sensing layer, b), which is caused by the presence of PVdF and the glass fiber substrate. They show specific IR bands at  $1211\text{ cm}^{-1}$ ,  $1184\text{ cm}^{-1}$  (PVdF) and  $1015\text{ cm}^{-1}$  (glass fiber).

To additionally confirm that the manganese has been sufficiently leached out from the  $\text{Mn(II)-IIP}$  complex during the sensing layer preparation, we measured the amount of manganese by ICP-MS. In this case, the manganese concentration found in the unleached  $\text{Mn(II)-IIP}$  sample was  $1.2\text{ mg L}^{-1}$ , whereas the concentration in the leached sample was below  $0.1\text{ mg L}^{-1}$ .

The redox activity of  $\text{Mn(II)-IIP}$  in the battery environment was

investigated by cyclic voltammetry. A glassy carbon (GC) disk was used as a supporting electrode for the  $\text{Mn(II)-IIP/PVdF}$  sensing material. Cyclic voltammograms of the unmodified GC disk and  $\text{Mn(II)-IIP/PVdF}$  modified GC disk in  $1.0\text{ M LiPF}_6$  in EC:DEC 1:1 electrolyte are shown in Figs. 3b and S5 (black line for GC, blue line for  $\text{Mn(II)-IIP/PVdF/GC}$ ). Due to the absence of any distinct signals during the cathodic and anodic scans, we can conclude that there is no electrochemical reaction between the  $\text{Mn(II)-IIP}$  composite and electrolyte in the operating voltage range for the LMO cells. The sensing layer is electrochemically stable and suitable for application in a battery cell.

In continuation, a similar measurement setup was used to understand the behavior of the polymer  $\text{Mn(II)-IIP}$  in the presence of manganese ions in the electrolyte, i.e., after the addition of  $\text{Mn(AcAc)}_2$ . Electrochemistry of  $\text{Mn(AcAc)}_2$  has already been evaluated in various electrolytes and with different electrode materials [55–57]. The cyclic voltammograms of the unmodified GC and  $\text{Mn(II)-IIP/PVdF}$  modified GC electrodes in the solution of  $10.0\text{ mM Mn(AcAc)}_2$  in  $1.0\text{ M LiPF}_6$  in EC:DEC 1:1 (wt:wt) electrolyte are presented in Fig. 3b (dotted orange line for the unmodified GC and red line for  $\text{Mn(II)-IIP/PVdF}$  modified GC). Both voltammograms revealed two well-defined redox couples during cyclic voltammetric scans. We can assign the signals a/a\* (at the unmodified GC) and 1/1\* (at the modified GC) to the  $\text{Mn}^{2+}/\text{Mn}^{3+}$  redox couple, and the signals b/b\* (at the unmodified GC) and 2/2\* (at the modified GC) to the  $\text{Mn}^{3+}/\text{Mn}^{4+}$  redox couple. We observed a shift of the anodic signal 1 towards higher potential and a shift of the cathodic signal 1\* towards the lower potential for the cell with  $\text{Mn(II)-IIP/PVdF}$  modified GC electrode in comparison to the unmodified GC electrode. Higher polarization between the oxidation/reduction process of the  $\text{Mn}^{\text{II}}/\text{Mn}^{\text{III}}$  couple in the presence of the  $\text{Mn(II)-IIP}$  indicates possible coordination of the manganese(II) species in the  $\text{Mn(II)-IIP}$  structure and conceivably slower diffusion pattern to the electrode surface.

To exclude the interference of the sensor with the electrochemistry of the LMO||Li battery cell, we assembled two test cells, one with added sensor and one conventional to be run in parallel. In one cell, the sensor printed on a glass fiber separator was positioned between two Celgard™

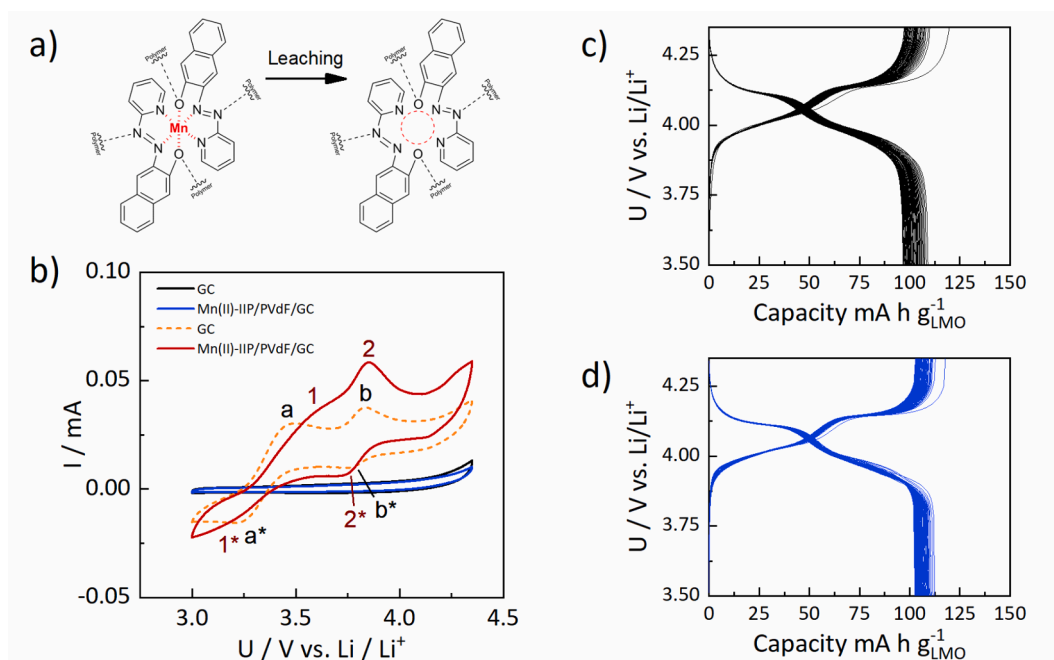


**Fig. 3.** Sensor and battery stability. (a) Chemical structures of the  $\text{Mn(II)-IIP}$  bonding site with and without trapped manganese ion; (b) cyclic voltammograms in  $1.0\text{ M LiPF}_6$  in EC:DEC 1:1 (wt:wt) (black and blue curves) and in  $10.0\text{ mM Mn(AcAc)}_2$  in  $1.0\text{ M LiPF}_6$  in EC:DEC 1:1 (wt:wt) (orange and red curves) at a scan rate of  $10\text{ mV s}^{-1}$ ; GC (black, orange) and  $\text{Mn(II)-IIP/PVdF/GC}$  (blue, red) were used as working electrodes, and lithium metal as counter and reference electrode; peak positions: a/a\*  $3.45/3.25\text{ V}$ , b/b\*  $3.85/3.75\text{ V}$ ; 1/1\*  $3.55/3.20\text{ V}$ , 2/2\*  $3.85/3.75\text{ V}$ ; charge and discharge voltage profiles of (c) LMO|celgard-glass fiber separator-celgard|Li and (d) LMO|celgard-sensor-celgard|Li at  $0.33\text{ C}$  in the voltage range of  $3.50\text{ V}$  to  $4.35\text{ V}$  vs  $\text{Li/Li}^+$  for 75 cycles.

2320 separators (Fig. S6), and in the second cell, a pristine glass fiber separator sheet was used. The cells were opened after cycling and the sensor morphology was checked with SEM (Fig. S7), where no detectable degradation or changes in the sensor's surface were observed. The cycling voltage profiles of the two LMO||Li battery cells are shown in Fig. 3c and d. The voltage profiles in both cases show two-step flat plateaus related to the two-stage process of  $\text{Li}^+$  removal/insertion without any measurable polarization or additional electrochemical signature that could be correlated to the presence of the sensor. As the comparable capacity fading was observed for both cells, we can confirm that the electrochemical sensor is stable and has no detrimental impact on the LMO||Li battery cell performance.

Further, we used electrochemical impedance spectroscopy (EIS) as a possible method of choice for the quantitative and qualitative detection of changes in the resistance of the sensing layer. This powerful analytical method is capable of characterizing physicochemical processes with different time constants. Obtained results suggest that the coordination of manganese ion within the Mn(II)-IIP-based material alters the impedance of the sensing layer (Fig. 4) in the mid-frequency range. To explain the working principle of the sensor we employ a transmission line model, which relates the conducting species and their interactions with the sensor. Fig. 4a presents the circuit describing the sensor interaction with the electrolyte without manganese ions. For easier model/material system correlation, the circuit is drawn on top of a schematic cross-section of the sensing electrodes (see the experimental cross-section image in Fig. 1c for reference). The circuit includes two parallel rails, one for the transport of electrons through the Mn(II)-IIP/MWCNT/PVdF sensing layer (upper rail, elements  $R_e$ ) and one for the transport of electrolyte ions through the electrolyte-filled glass fiber substrate (lower rail, elements  $R_i$ ). The terminal ends of both rails describe the interaction of the transporting species with the sensor's

glassy carbon-printed electrodes. For electrons, this is a resistive element  $R_{\text{int}}$  and for ions, a capacitor element  $C_{\text{dl},1}$ . Both rails are connected with vertical capacitor elements that describe the interaction of ions with the sensing layer. Since no manganese ions are present, the interaction of electrolyte ions with the sensing layer is nonspecific and constitutes a capacitor element  $C_{\text{dl},2}$ . Such a circuit produces a spectrum with three distinct features – a resistive intercept ( $R_{\text{intercept}}$ , see Eq. (1)), a high-frequency arc  $R_{\text{int}}$  with a capacitance of  $C_{\text{dl},1}$ , and a low-frequency feature with a Warburg arc shape with a transmissive boundary that has a resistance size of  $R_w$  (Eq. (2)).

$$R_{\text{intercept}} = \frac{R_e R_i}{R_e + R_i} \quad (1)$$

$$R_w = R_e - \frac{R_e R_i}{R_e + R_i} \quad (2)$$

To prove the concept of the developed sensor functioning we performed impedance spectra measurements of sensors soaked with electrolyte without or with manganese ions (Fig. 4). Fig. 4b shows the impedance response of the sensor wetted by 200  $\mu\text{L}$  of 1.0 M  $\text{LiPF}_6$  in EC:DEC 1:1 and packed it in a protective pouch cell casing. The measurement was performed in the frequency range of 1 MHz to 10 mHz. The first EIS spectrum was measured 30 min after electrolyte addition, whereas the measurements were repeated for several hours. The impedance response corresponds well to the physical model. The evaluation of EIS spectra unveiled only slight and negligible changes in the impedance resistance and capacitance values over time.

When an electrolyte contains manganese ions, the inherent model for the electrochemical behavior of the sensor changes (Fig. 4c); in this case, the vertical elements have to contain specific interactions of the manganese ions in the electrolyte with the sensing material, meaning that to

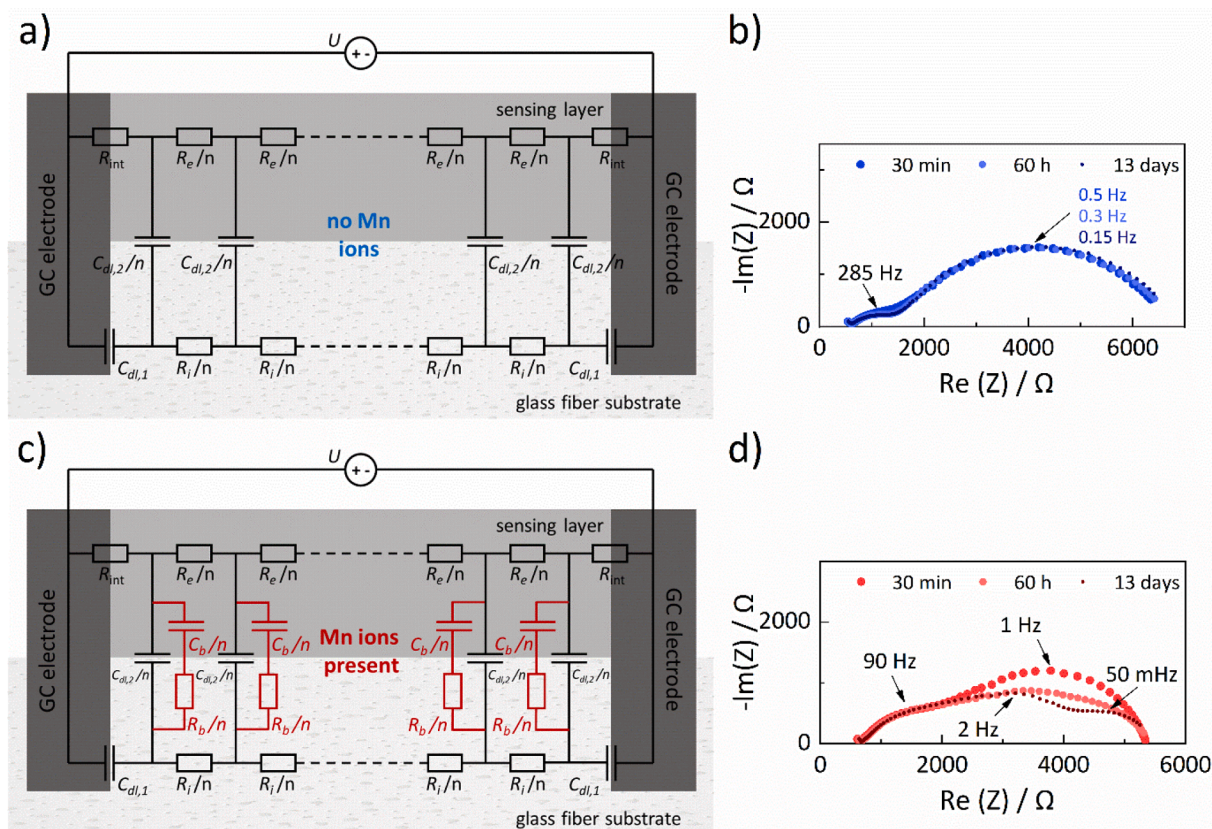


**Fig. 4.** Sensor response. (a) Transmission line model for the description of the impedance response of the printed sensor without manganese ions in the electrolyte, (b) sensor impedance response and its change with time in 1.0 M  $\text{LiPF}_6$  in EC:DEC 1:1 (wt:wt), (c) as (a) with an electrolyte containing 10.0 mM  $\text{Mn}(\text{AcAc})_2$ , and (d) as (b) containing 10.0 mM  $\text{Mn}(\text{AcAc})_2$  in the electrolyte.

the previous  $C_{dl,2}$  capacitor are added in parallel two circuit elements in series, i.e.,  $R_b$  and  $C_b$ , describing the specific binding interaction [58]. Due to the addition of the two elements  $R_b$  and  $C_b$  in the vertical connections between the rails, the features in the EIS spectrum are severely complicated in comparison to the features described for the case without manganese ions. This is in line with the features present in the recorded EIS spectra in Fig. 4d. The experiment was conducted by adding 200  $\mu$ L of 10.0 mM  $Mn(AcAc)_2$  in 1.0 M  $LiPF_6$  in EC:DEC 1:1 (wt:wt) electrolyte to the sensor and measuring impedance spectra in the same way as in the case of the sensor without manganese ions in the electrolyte.

Fig. 4d shows the evolution of the spectra features over time. In this case, the initial spectra are similar in size and shape to the spectra measured with sensors that were not in contact with manganese ions. Over time, the features changed, producing three distinct arcs. The first changes in the EIS spectra were detected after 10 h. These alterations can only be attributed to the change in the sensor's electrochemical behavior due to the addition of manganese ions. To additionally confirm this, we checked the influence of acetylacetonate anions separately. When the same set of impedance spectra measurements was performed by adding 200  $\mu$ L of 20.0 mM  $LiAcAc$  in 1.0 M  $LiPF_6$  in EC:DEC 1:1 electrolyte, the EIS spectra showed negligible changes over time (Fig. S8). Therefore, these experiments corroborate that the developed sensor can specifically detect the presence of manganese ions.

### 3.3. Detection of soluble manganese in LMO||Li cell

The combination of printing electrodes on the separator, sensing layer, and the capability of EIS to follow changes in the resistance/capacitance behavior of the sensing layer offers a convenient and reliable methodology for the detection of SoH in Li-ion batteries without the need for significant modification of the cell production process, and most importantly, without affecting the cell performance. We assembled

several cells with a printed sensor on the separator between the LMO cathode and metallic lithium anode, and the cells were cycled with different current densities. Fig. 5 shows two cells, one cycled at 0.33 C (Fig. 5a) and another at 0.1 C (Fig. 5c). Changes in the corresponding impedance spectra shape are similar to those observed in Fig. 4d. Changes are more pronounced in the experiment where cells were cycled with a slower C-rate (Fig. 5c and d). The reason for that can be the slow kinetics of manganese adsorption/coordination within the Mn(II)-IIP/MWCNT/PVdF sensing layer composite and/or larger amount of dissolved manganese due to longer exposure of the cell to high voltages. Both cells showed typical patterns in the EIS spectra, which can be attributed to the changes in the sensing layer due to adsorption/coordination of dissolved manganese cations within the Mn(II)-IIP/MWCNT/PVdF composite. Measured EIS spectra can be well described with a transmission line model shown in Fig. 4c.

Further optimization of the sensor is required to enable a quantitative detection of dissolved manganese. This can be obtained by preparing the sensing layer under more controlled conditions; the possible direction might be the application of printing technology together with the adjustment of ink quality and printing parameters. The potential issue of the slow kinetics of manganese adsorption/coordination in the Mn(II)-IIP/MWCNT/PVdF sensing layer will be further investigated by using different coordination compounds and by optimizing the morphology of the sensing layer.

## 4. Conclusions

In this work, we demonstrate an integrated sensor printed on the separator that enables convenient detection of dissolved manganese ions in the battery cell. The operation principle is based on the resistance change due to different physicochemical properties of the sensing composite layer before and after coordination with manganese; the

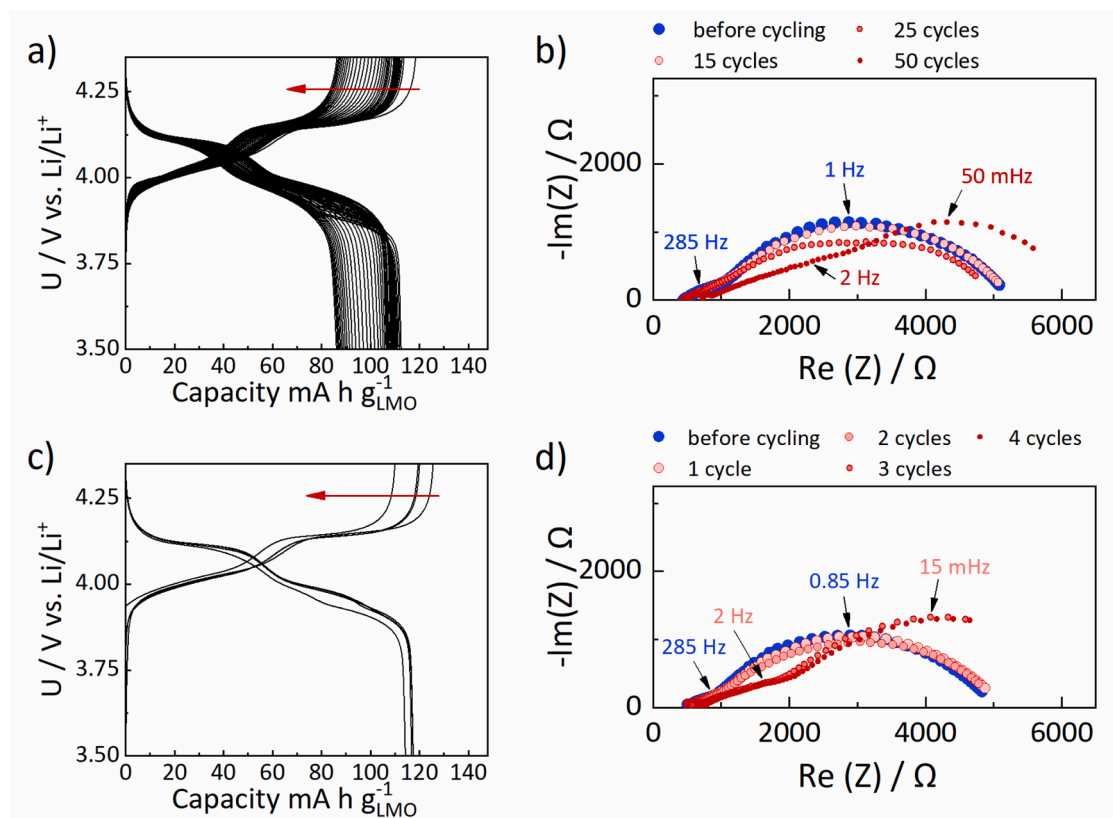


**Fig. 5.** *In-situ* detection of dissolved manganese. (a) Charge and discharge voltage profiles of LMO|celgard-sensor-celgard|Li cells at 0.33 C in the voltage range of 3.50 V to 4.35 V vs  $Li/Li^+$  for 50 cycles and (b) related cycle evaluation of the impedance response; (c) as (a) at 0.1 C in the voltage range of 3.50 V to 4.35 V vs  $Li/Li^+$  for 4 cycles and (d) as (b) at 0.1 C.

change can be monitored by the electrochemical impedance spectroscopy in the mid-frequency range. This is demonstrated with a manganese ion-imprinted polymer (Mn(II)-IIP)-based sensing composite layer deposited between two electrodes printed on the separator. The sensing composite is selective to divalent cations. The newly developed sensor is stable in a Li-ion battery environment and can be easily scaled up. The sensor's operation was successfully demonstrated in the single-layer pouch cells using LMO||Li chemistry at two different C-rates, exhibiting promising performances for its future application in monitoring the battery's health, safety, and lifetime parameters.

The proposed sensor enables the detection of dissolved manganese, however, that has to be demonstrated in the full-cell configuration. Some remaining concerns will be tested and evaluated in near future. Within this study, we did not evaluate long-term stability and sensibility in the full-cell configuration. Further, additional research activities are going on the check if the sensor has the capability of quantification of dissolved manganese. Based on the continuous change of EIS signal that is expected, but it has to be carefully examined. Considerably more work will need to be done in this area. Within this work, we proposed one geometry with a selected sensing layer, however, the use of a different geometry or a different sensing layer composition can lead in simplification of detection where a final goal is to replace EIS with simple measurement of ohmic resistance.

### CRedit authorship contribution statement

**Tina Paljk:** Conceptualization, Methodology, Formal analysis, Investigation, Formal analysis, Visualization. **Victoria Bracamonte:** Conceptualization, Methodology, Writing – original draft. **Tomáš Syrový:** Conceptualization, Methodology, Formal analysis, Writing – original draft. **Sara Drvarič Talian:** Formal analysis, Writing – original draft. **Samo Hočevar:** Formal analysis, Writing – review & editing. **Robert Dominko:** Conceptualization, Methodology, Investigation, Formal analysis, Supervision, Writing – review & editing, Project administration, Funding acquisition.

### Declaration of Competing Interest

The authors declare that they have no known competing financial interests or personal relationships that could have appeared to influence the work reported in this paper.

### Data availability

Data will be made available on request.

### Acknowledgment

The authors acknowledge the financial support from the Slovenian Research Agency young researcher scheme and research core funding [P2-0393], [P1-0034], and [P2-0423] and project [N2-0214]. The financial support received from the European Union's Horizon 2020 research and innovation program under the grant agreement [957213] (Battery 2030PLUS) is acknowledged. The work was also supported by the European Regional Development Fund-Project "Organic redox couple-based batteries for the energetics of traditional and renewable resources (ORGBAT)" [CZ.02.1.01/0.0/ 0.0/16\_025/0007445]. The authors acknowledge a fruitful discussion with dr. Chernychova and dr. Vizintin for his expertise and assistance in IR spectroscopy measurements.

### Supplementary materials

Supplementary material associated with this article can be found, in the online version, at doi:10.1016/j.ensm.2022.11.039.

### References

- [1] M. Bercibar, Machine-learning techniques used to accurately predict battery life, *Nature* 568 (2019) 325–326, <https://doi.org/10.1038/d41586-019-01138-1>.
- [2] J. Huang, S.T. Boles, J.M. Tarascon, Sensing as the key to battery lifetime and sustainability, *Nat. Sustain.* 5 (2022) 194–204, <https://doi.org/10.1038/s41893-022-00859-y>.
- [3] M. Fichtner, K. Edström, E. Ayerbe, M. Bercibar, A. Bhowmik, I.E. Castelli, S. Clark, R. Dominko, M. Erakca, A.A. Franco, A. Grimaud, B. Horstmann, A. Latz, H. Lorrman, M. Meeus, R. Narayan, F. Pammer, J. Ruhland, H. Stein, T. Vegge, M. Weil, Rechargeable batteries of the future—the state of the art from a BATTERY 2030<sup>+</sup> perspective, *Adv. Energy Mater.* 12 (2022), 2102904, <https://doi.org/10.1002/aenm.202102904>.
- [4] A.M. Tripathi, W.N. Su, B.J. Hwang, *In situ* analytical techniques for battery interface analysis, *Chem. Soc. Rev.* 47 (2018) 736–851, <https://doi.org/10.1039/C7CS00180K>.
- [5] D. Liu, Z. Shadik, R. Lin, K. Qian, H. Li, K. Li, S. Wang, Q. Yu, M. Liu, S. Ganapathy, X. Qin, Q. Yang, M. Wagemaker, F. Kang, X. Yang, B. Li, Review of recent development of *in situ*/operando characterization techniques for lithium battery research, *Adv. Mater.* 31 (2019), 1806620, <https://doi.org/10.1002/adma.201806620>.
- [6] L. Meyer, N. Saqib, J. Porter, Review-operando optical spectroscopy studies of batteries, *J. Electrochem. Soc.* 168 (2021), 090561, <https://doi.org/10.1149/1945-7111/ac2088>.
- [7] W. Li, D.M. Lutz, L. Wang, K.J. Takeuchi, A.C. Marschilok, E.S. Takeuchi, Peering into batteries: electrochemical insight through *in situ* and operando methods over multiple length scales, *Joule* 5 (2021) 77–88, <https://doi.org/10.1016/j.joule.2020.11.003>.
- [8] X. Lu, J.M. Tarascon, J. Huang, Perspective on commercializing smart sensing for batteries, *eTransportation* 14 (2022), 100207, <https://doi.org/10.1016/j.etrans.2022.100207>.
- [9] C.P. Grey, J.M. Tarascon, Sustainability and *in situ* monitoring in battery development, *Nat. Mater.* 16 (2017) 45–56, <https://doi.org/10.1038/nmat4777>.
- [10] J. Huang, L. Albero Blanquer, J. Bonafacino, E.R. Logan, D. Alves Dalla Corte, C. Delacourt, B.M. Gallant, S.T. Boles, J.R. Dahn, H.Y. Tam, J.M. Tarascon, Operando decoding of chemical and thermal events in commercial Na(Li)-ion cells via optical sensors, *Nat. Energy* 5 (2020) 674–683, <https://doi.org/10.1038/s41560-020-0665-y>.
- [11] M. Nascimento, T. Paixão, M. Ferreira, J. Pinto, Thermal mapping of a lithium polymer batteries pack with FBGs network, *Batteries* 4 (2018) 67, <https://doi.org/10.3390/batteries4040067>.
- [12] A. Raghavan, P. Kiesel, L.W. Sommer, J. Schwartz, A. Lochbaum, A. Hegyi, A. Schuh, K. Arakaki, B. Saha, A. Ganguli, K.H. Kim, C. Kim, H.J. Hah, S. Kim, G. O. Hwang, G.C. Chung, B. Choi, M. Alamgir, Embedded fiber-optic sensing for accurate internal monitoring of cell state in advanced battery management systems part 1: cell embedding method and performance, *J. Power Sources* 341 (2017) 466–473, <https://doi.org/10.1016/j.jpowsour.2016.11.104>.
- [13] J. Huang, L.A. Blanquer, C. Gervillie, J.M. Tarascon, Distributed fiber optic sensing to assess in-live temperature imaging inside batteries: rayleigh and FBGs, *J. Electrochem. Soc.* 168 (2021), 060520, <https://doi.org/10.1149/1945-7111/ac03f0>.
- [14] M.S.K. Mutyala, J. Zhao, J. Li, H. Pan, C. Yuan, X. Li, *In-situ* temperature measurement in lithium ion battery by transferable flexible thin film thermocouples, *J. Power Sources* 260 (2014) 43–49, <https://doi.org/10.1016/j.jpowsour.2014.03.004>.
- [15] J. Fleming, T. Amietszajew, J. Charmet, A.J. Roberts, D. Greenwood, R. Bhagat, The design and impact of *in-situ* and operando thermal sensing for smart energy storage, *J. Energy Storage* 22 (2019) 36–43, <https://doi.org/10.1016/j.est.2019.01.026>.
- [16] A. Knobloch, C. Kapusta, J. Karp, Y. Plotnikov, J.B. Siegel, A.G. Stefanopoulou, Fabrication of multimeasurand sensor for monitoring of a Li-ion battery, *J. Electron. Packag.* 140 (2018), <https://doi.org/10.1115/1.4039861>.
- [17] Z. Li, J. Zhang, B. Wu, J. Huang, Z. Nie, Y. Sun, F. An, N. Wu, Examining temporal and spatial variations of internal temperature in large-format laminated battery with embedded thermocouples, *J. Power Sources* 241 (2013) 536–553, <https://doi.org/10.1016/j.jpowsour.2013.04.117>.
- [18] J. Singer, C. Sämann, T. Gössl, K. Birke, Pressure monitoring cell for constrained battery electrodes, *Sensors* 18 (2018) 3808, <https://doi.org/10.3390/s18113808>.
- [19] A.J. Louli, L.D. Ellis, J.R. Dahn, Operando pressure measurements reveal solid electrolyte interphase growth to rank Li-ion cell performance, *Joule* 3 (2019) 745–761, <https://doi.org/10.1016/j.joule.2018.12.009>.
- [20] J. Zhu, J. Feng, L. Lu, K. Zeng, *In situ* study of topography, phase and volume changes of titanium dioxide anode in all-solid-state thin film lithium-ion battery by biased scanning probe microscopy, *J. Power Sources* 197 (2012) 224–230, <https://doi.org/10.1016/j.jpowsour.2011.08.115>.
- [21] J. Lao, P. Sun, F. Liu, X. Zhang, C. Zhao, W. Mai, T. Guo, G. Xiao, J. Albert, *In situ* plasmonic optical fiber detection of the state of charge of supercapacitors for renewable energy storage, *Light Sci. Appl.* 7 (2018) 34, <https://doi.org/10.1038/s41377-018-0040-y>.
- [22] B. Sood, M. Osterman, M. Pecht, Health monitoring of lithium-ion batteries, in: proceedings of the IEEE Symposium on Product Compliance Engineering (ISPC), IEEE, 2013, pp. 1–6, <https://doi.org/10.1109/ISPC.2013.6664165>.
- [23] R. Dominko, R. Demir-Cakan, M. Morcrette, J.M. Tarascon, Analytical detection of soluble polysulphides in a modified Swagelok cell, *Electrochem. Commun.* 13 (2011) 117–120, <https://doi.org/10.1016/j.elecom.2010.11.029>.

- [24] J. Wang, M.M. Islam, S.W. Donne, *In-situ* detection of  $\text{LiMn}_2\text{O}_4$  dissolution during electrochemical cycling by, *Electrochim. Acta* 386 (2021), 138366, <https://doi.org/10.1016/j.electacta.2021.138366>.
- [25] F. Linsenmann, D. Pritzl, H.A. Gasteiger, A reference electrode for *in situ* impedance measurements in sodium-ion batteries, *J. Electrochem. Soc.* 166 (2019) A3668–A3674, <https://doi.org/10.1149/2.0741915jes>.
- [26] H. Beitollahi, S.Z. Mohammadi, M. Safaei, S. Tajik, Applications of electrochemical sensors and biosensors based on modified screen-printed electrodes: a review, *Anal. Methods* 12 (2020) 1547–1560, <https://doi.org/10.1039/C9AY02598G>.
- [27] M. Wohlfahrt-Mehrens, C. Vogler, J. Garche, Aging mechanisms of lithium cathode materials, *J. Power Sources* 127 (2004) 58–64, <https://doi.org/10.1016/j.jpowsour.2003.09.034>.
- [28] C. Zhan, T. Wu, J. Lu, K. Amine, Dissolution, migration, and deposition of transition metal ions in Li-ion batteries exemplified by Mn-based cathodes – a critical review, *Energy Environ. Sci.* 11 (2018) 243–257, <https://doi.org/10.1039/C7EE03122J>.
- [29] A. Bhandari, J. Bhattacharya, Review—manganese dissolution from spinel cathode: few unanswered questions, *J. Electrochem. Soc.* 164 (2017) A106–A127, <https://doi.org/10.1149/2.0101614jes>.
- [30] J.C. Hunter, Preparation of a new crystal form of manganese dioxide:  $\lambda$ - $\text{MnO}_2$ , *J. Solid State Chem.* 39 (1981) 142–147, [https://doi.org/10.1016/0022-4596\(81\)90323-6](https://doi.org/10.1016/0022-4596(81)90323-6).
- [31] R.J. Gummow, A. de Kock, M.M. Thackeray, Improved capacity retention in rechargeable 4V lithium/lithium-manganese oxide (spinel) cells, *Solid State Ion.* 69 (1994) 59–67, [https://doi.org/10.1016/0167-2738\(94\)90450-2](https://doi.org/10.1016/0167-2738(94)90450-2).
- [32] J.M. Tarascon, E. Wang, F.K. Shokoohi, W.R. McKinnon, S. Colson, The spinel phase of  $\text{LiMn}_2\text{O}_4$  as a cathode in secondary lithium cells, *J. Electrochem. Soc.* 138 (1991) 2859–2864, <https://doi.org/10.1149/1.2085330>.
- [33] J.M. Tarascon, D. Guyomard, The  $\text{Li}^{1+x}\text{Mn}_2\text{O}_4/\text{C}$  rocking-chair system: a review, *Electrochim. Acta* 38 (1993) 1221–1231, [https://doi.org/10.1016/0013-4686\(93\)80053-3](https://doi.org/10.1016/0013-4686(93)80053-3).
- [34] C.H. Lu, S.W. Lin, Dissolution kinetics of spinel lithium manganate and its relation to capacity fading in lithium ion batteries, *J. Mater. Res.* 17 (2002) 1476–1481, <https://doi.org/10.1557/JMR.2002.0219>.
- [35] Y. Xia, Y. Zhou, M. Yoshio, Capacity fading on cycling of 4V Li /  $\text{LiMn}_2\text{O}_4$  cells, *J. Electrochem. Soc.* 144 (1997) 2593–2600, <https://doi.org/10.1149/1.1837870>.
- [36] A. Banerjee, Y. Shilina, B. Ziv, J.M. Ziegelbauer, S. Luski, D. Aurbach, I.C. Halalay, On the oxidation state of manganese ions in Li-ion battery electrolyte solutions, *J. Am. Chem. Soc.* 139 (2017) 1738–1741, <https://doi.org/10.1021/jacs.6b10781>.
- [37] D. Tang, Y. Sun, Z. Yang, L. Ben, L. Gu, X. Huang, Surface structure evolution of  $\text{LiMn}_2\text{O}_4$  cathode material upon charge/discharge, *Chem. Mater.* 26 (2014) 3535–3543, <https://doi.org/10.1021/cm501125e>.
- [38] Y. Terada, Y. Nishiwaki, I. Nakai, F. Nishikawa, Study of Mn dissolution from  $\text{LiMn}_2\text{O}_4$  spinel electrodes using *in situ* total reflection X-ray fluorescence analysis and fluorescence XAFS technique, *J. Power Sources* 97–98 (2001) 420–422, [https://doi.org/10.1016/S0378-7753\(01\)00741-8](https://doi.org/10.1016/S0378-7753(01)00741-8).
- [39] L.F. Wang, C.C. Ou, K.A. Striebel, J.S. Chen, Study of Mn dissolution from  $\text{LiMn}_2\text{O}_4$  spinel electrodes using rotating ring-disk collection experiments, *J. Electrochem. Soc.* 150 (2003) A905, <https://doi.org/10.1149/1.1577543>.
- [40] L. Zhao, E. Chénard, Ö.Ö. Çapraz, N.R. Sottos, S.R. White, Direct detection of manganese ions in organic electrolyte by UV-Vis spectroscopy, *J. Electrochem. Soc.* 165 (2018) A345–A348, <https://doi.org/10.1149/2.1111802jes>.
- [41] L. Hanf, J. Henschel, M. Diehl, M. Winter, S. Nowak,  $\text{Mn}^{2+}$  or  $\text{Mn}^{3+}$ ? Investigating transition metal dissolution of manganese species in lithium ion battery electrolytes by capillary electrophoresis, *Electrophoresis* 41 (2020) 697–704, <https://doi.org/10.1002/elps.201900443>.
- [42] S. Nikman, D. Zhao, V. Gonzalez-Perez, H.E. Hoster, S.F.L. Mertens, Surface or bulk? Real-time manganese dissolution detection in a lithium-ion cathode, *Electrochim. Acta* 386 (2021), 138373, <https://doi.org/10.1016/j.electacta.2021.138373>.
- [43] Z. Koudelkova, T. Syrový, P. Ambrozova, Z. Moravec, L. Kubac, D. Hynek, L. Richtera, V. Adam, Determination of zinc, cadmium, lead, copper and silver using a carbon paste electrode and a screen printed electrode modified with chromium(III) oxide, *Sensors* 17 (2017) 1832, <https://doi.org/10.3390/s17081832>.
- [44] P. Kuberský, T. Syrový, A. Hamáček, S. Nešpůrek, L. Syrová, Towards a fully printed electrochemical  $\text{NO}_2$  sensor on a flexible substrate using ionic liquid based polymer electrolyte, *Sens. Actuators B Chem.* 209 (2015) 1084–1090, <https://doi.org/10.1016/j.snb.2014.12.116>.
- [45] L. Gillan, E. Jansson, Molecularly imprinted polymer on roll-to-roll printed electrodes as a single use sensor for monitoring of cortisol in sweat, *Flexible and Printed Electronics*. 7 (2022), 025014, <https://doi.org/10.1088/2058-8585/ac7187>.
- [46] M. Bariya, Z. Shahpar, H. Park, J. Sun, Y. Jung, W. Gao, H.Y.Y. Nyein, T.S. Liaw, L. C. Tai, Q.P. Ngo, M. Chao, Y. Zhao, M. Hettick, G. Cho, A. Javey, Roll-to-roll gravure printed electrochemical sensors for wearable and medical devices, *ACS Nano* 12 (2018) 6978–6987, <https://doi.org/10.1021/acsnano.8b02505>.
- [47] A.M. Ulloa, N. Glassmaker, M.R. Odunccu, P. Xu, A. Wei, M. Cakmak, L. Stanciu, Roll-to-roll manufactured sensors for nitroaromatic organophosphorus pesticides detection, *ACS Appl. Mater. Interfaces* 13 (2021) 35961–35971, <https://doi.org/10.1021/acami.1c08700>.
- [48] D.L. Wood, M. Wood, J. Li, Z. Du, R.E. Ruther, K.A. Hays, N. Muralidharan, L. Geng, C. Mao, I. Belharouk, Perspectives on the relationship between materials chemistry and roll-to-roll electrode manufacturing for high-energy lithium-ion batteries, *Energy Storage Mater.* 29 (2020) 254–265, <https://doi.org/10.1016/j.ensm.2020.04.036>.
- [49] M. Roushani, Z. Saedi, F. Hamdi, B.Z. Dizajdizi, Preparation an electrochemical sensor for detection of manganese (II) ions using glassy carbon electrode modified with multi walled carbon nanotube-chitosan-ionic liquid nanocomposite decorated with ion imprinted polymer, *J. Electroanal. Chem.* 804 (2017) 1–6, <https://doi.org/10.1016/j.jelechem.2017.09.038>.
- [50] J.A. Gilbert, I.A. Shkrob, D.P. Abraham, Transition metal dissolution, ion migration, electrocatalytic reduction and capacity loss in lithium-ion full cells, *J. Electrochem. Soc.* 164 (2017) A389–A399, <https://doi.org/10.1149/2.1111702jes>.
- [51] C. Zhan, J. Lu, A. Jeremy Kropf, T. Wu, A.N. Jansen, Y.K. Sun, X. Qiu, K. Amine, Mn (II) deposition on anodes and its effects on capacity fade in spinel lithium manganate-carbon systems, *Nat. Commun.* 4 (2013) 2437, <https://doi.org/10.1038/ncomms3437>.
- [52] D.H. Jang, S.M. Oh, Electrolyte effects on spinel dissolution and cathodic capacity losses in 4V Li / Li x  $\text{Mn}_2\text{O}_4$  rechargeable cells, *J. Electrochem. Soc.* 144 (1997) 3342–3348, <https://doi.org/10.1149/1.1838016>.
- [53] T. Inoue, M. Sano, An investigation of capacity fading of manganese spinels stored at elevated temperature, *J. Electrochem. Soc.* 145 (1998) 3704–3707, <https://doi.org/10.1149/1.1838862>.
- [54] Y. Tesfamhret, H. Liu, Z. Chai, E. Berg, R. Younesi, On the manganese dissolution process from  $\text{LiMn}_2\text{O}_4$  cathode materials, *ChemElectroChem* 8 (2021) 1516–1523, <https://doi.org/10.1002/celec.202001496>.
- [55] E. Bouwman, R. van Gorkum, A study of new manganese complexes as potential driers for alkyd paints, *J. Coat. Technol. Res.* 4 (2007) 491–503, <https://doi.org/10.1007/s11998-007-9041-0>.
- [56] S. Carli, E. Benazzi, L. Casarin, T. Bernardi, V. Bertolasi, R. Argazzi, S. Caramori, C. A. Bignozzi, On the stability of manganese tris( $\beta$ -diketonate) complexes as redox mediators in DSSCs, *Phys. Chem. Chem. Phys.* 18 (2016) 5949–5956, <https://doi.org/10.1039/C5CP05524E>.
- [57] M.H. Chakrabarti, N.P. Brandon, F.S. Mjalli, L. Bahadori, I.M. al Nashef, M. A. Hashim, M.A. Hussain, C.T.J. Low, V. Yufit, Cyclic voltammetry of metallic acetylacetonate salts in quaternary ammonium and phosphonium based deep eutectic solvents, *J. Solut. Chem.* 42 (2013) 2329–2341, <https://doi.org/10.1007/s10953-013-0111-x>.
- [58] A. Lasia, Electrochemical impedance spectroscopy and its applications, in: *Modern Aspects of Electrochemistry*, Kluwer Academic Publishers, Boston, n.d.: pp. 143–248. [10.1007/0-306-46916-2.2](https://doi.org/10.1007/0-306-46916-2.2).